



Cite this: *Soft Matter*, 2017, 13, 4305

Received 8th May 2017,
Accepted 24th May 2017

DOI: 10.1039/c7sm00917h

rsc.li/soft-matter-journal

Electro-elastocapillary Rayleigh–plateau instability in dielectric elastomer films†

Saman Seifi^a and Harold S. Park^{*b}

We demonstrate, using both finite element simulations and a linear stability analysis, the emergence of an electro-elastocapillary Rayleigh–plateau instability in dielectric elastomer (DE) films under 2D, plane strain conditions. When subject to an electric field, the DEs exhibit a buckling instability for small elastocapillary numbers. For larger elastocapillary numbers, the DEs instead exhibit the Rayleigh–plateau instability. The stability analysis demonstrates the critical effect of the electric field in causing the Rayleigh–plateau instability, which cannot be induced solely by surface tension in DE films. Overall, this work demonstrates the effects of geometry, boundary conditions, and multi-physical coupling on a new example of Rayleigh–plateau instability in soft solids.

1 Introduction

The effects of surface tension on the behavior of fluids have been investigated for many years. The canonical example is the Rayleigh–plateau instability (RPI), in which a fluid breaks up into smaller drops in order to minimize its surface area while keeping the volume unchanged.¹ More recently, significant interest has developed in understanding the effects of surface tension on solids, and in particular soft solids like gels and elastomers^{2–4} through an effect known as elastocapillarity. The reason why surface tension only impacts soft solids can be gleaned through the elastocapillary length $l_e = \gamma/\mu$, where γ is the surface tension and μ is the solid shear modulus. While l_e is negligible for crystalline solids, it can approach macroscopic dimensions for soft solids with sufficiently small μ , which has resulted in many recent investigations of surface tension effects on the deformation of soft solids.^{2–5}

Recently, Mora *et al.*⁶ reported experimental observations of surface tension-induced RPI in soft gels, in which the gels exhibited capillary instabilities characterized by large, local area constrictions along the length of the gel. Subsequently, researchers have investigated various aspects of the RPI in soft solids.^{6–10} An important unresolved question, which we address here, is how the RPI in soft solids is impacted by non-mechanical external perturbations. Such questions may be relevant for soft solids like dielectric elastomers (DEs),^{11–13} which have been extensively studied in recent years due to their potential as a soft and flexible actuation material when

subject to externally applied electric fields. While many of the most interesting applications for DEs, such as soft, underwater robots,^{14,15} tunable lenses,¹⁶ manipulating microfluidic flows¹⁷ and magnetic resonance imaging,¹⁸ involve operation of the DE in fluidic environments, where elastocapillary effects due to the presence of a fluid may be prominent,^{2,5} elastocapillary effects can be felt by solids in the absence of a fluid, for example due to vacuum, gas or an interface with another soft solid.

Here, we demonstrate using a combination of nonlinear finite element (FE) methods¹⁹ and a rigorous linear stability analysis^{20,21} that a DE film subjected to electro-elastocapillary forces undergoes an instability transition from buckling to RPI. Our analytic model and FE calculations show the transition point between these two types of instabilities occurs at a critical elastocapillary number of $\bar{\gamma}_c = \gamma_c/\mu H \simeq 2$ and normalized electric potential $\bar{\Phi}_c = \Phi_c/H\sqrt{\epsilon/\mu} = 2$; these expressions are valid assuming that the DE film length L is much larger than its thickness H .

The problem schematic and the aforementioned instability transition are shown in Fig. 1. There, we consider a DE film that is fixed at both ends. We consider 2D, plane strain conditions for the DE film as the in-plane dimensions are typically much larger than the thickness¹³ for DEs. The bottom of the film is voltage-free, *i.e.* $\Phi = 0$, while the top of the film is subject to a time-dependent voltage $\Phi(t)$ which increases linearly with time, while surface tension γ acts on both the top and bottom surfaces. The increase in voltage is sufficiently slow such that the electrostatic loading process can be modeled analytically as quasi-static. The aspect ratio of the DE film is $L/H = 20$, which is modeled using standard bilinear 2D plane strain finite elements which fully account for incompressibility of the DE.²² The FE model used is dynamic, nonlinear, fully electromechanically coupled, and was previously shown to accurately capture

^a Department of Mechanical Engineering, Boston University, Boston, MA 02215, USA. E-mail: samansei@bu.edu

^b Department of Mechanical Engineering, Boston University, Boston, MA 02215, USA. E-mail: parkhs@bu.edu; Fax: +001 617 353 5866; Tel: +001 617 353 4208

† Electronic supplementary information (ESI) available. See DOI: 10.1039/c7sm00917h

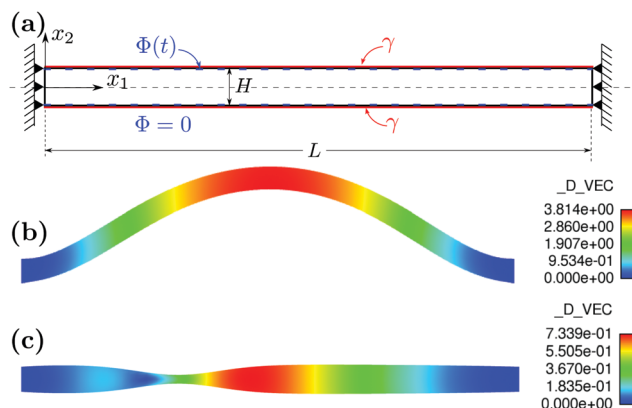


Fig. 1 (a) Schematic with boundary conditions for a DE film subjected to elastocapillary and electrical forces. (b and c) FE results showing different modes of instability. (b) Buckling for $\bar{\gamma} = 0.5$ where the critical voltage reaches $\bar{\Phi}_c = 1.066$. (c) RPI for $\bar{\gamma} = 5$ where the critical voltage is ramped up to $\bar{\Phi}_c = 2.03$. D_VEC refers to the displacement magnitude.

experimentally-observed²³ surface tension effects on surface instabilities like creasing and wrinkling of DEs.¹⁹

Fig. 1(b) demonstrates that at small elastocapillary numbers $\gamma/\mu H$, the DE film buckles once a critical voltage is reached. The buckling occurs because the DE film is fixed at both ends, which prevents both the elongation in the x_1 -direction and the contraction in the thickness (x_2)-direction that would otherwise occur due to the applied voltage,²⁴ leaving the DE in a state of axial compression. Eventually, as the compressive force increases due to increasing voltage, the film buckles as shown in Fig. 1(b). In contrast, for larger elastocapillary numbers, buckling is not observed, as shown in Fig. 1(c). Instead, a RPI-like instability is observed.

2 Electro-elastocapillary buckling

We now present an analytic model of the electro-elastocapillary buckling and RPI instabilities, which accounts for both surface tension, as well as the electromechanical coupling in the DE film due to the applied voltage. We first consider the voltage-induced buckling by considering a DE film with a rectangular cross section $H \times W$ subject to both electric field $\mathbf{E} = (E_1 \ E_2)^T$ and surface tension γ . For the DE film shown in Fig. 1(a), the modified buckling equation assuming quasistatic loading while accounting for surface tension and electric fields can be written as

$$YI \frac{\partial^4 u_2}{\partial x_1^4} + (P - P_s) \frac{\partial^2 u_2}{\partial x_1^2} = 0 \quad (1)$$

where Y is the Young's modulus, $u_2(x_1)$ denotes the vertical deflection at point x_1 , and $P_s = 2\gamma W$ is the axial force due to surface tension, which depends upon the surface tension γ and the out of plane (z -direction) width W of the film.^{25,26} P is the axial force that is generated by the application of an electric field in the x_2 -direction ($E_1 = 0$)

$$P = \epsilon E_2^2 A \quad (2)$$

where $A = HW$ is the cross sectional area. According to Euler buckling theory, the critical load of axial buckling can be found as

$$P_c = \eta \frac{\pi^2 YI}{L^2} + P_s \quad (3)$$

Inserting $E_2 = -\Phi/H$ for Φ the applied voltage on top of the beam and H being the height, the critical voltage can be found as

$$\bar{\Phi}_c = H \left(\frac{\mu}{\epsilon} \right)^{-1/2} \sqrt{\eta \frac{\pi^2 YH^2}{12L^2\mu} + 2 \frac{\gamma}{\mu H}} \quad (4)$$

where ϵ is the dielectric constant. Normalizing the voltage by $H\sqrt{\mu/\epsilon}$ and the surface tension by μH we obtain the relationship between critical voltage $\bar{\Phi}_c$ and elastocapillary number $\bar{\gamma} = \gamma/\mu H$ for a film with both ends fixed ($\eta = 4$) as

$$\bar{\Phi}_c = \sqrt{\frac{\pi^2 YH^2}{3L^2\mu} + 2\bar{\gamma}} \quad (5)$$

3 Electro-elastocapillary Rayleigh–plateau instability

3.1 Governing equations and their incremental forms

However, as shown in Fig. 1, the instability mechanism changes for elastocapillary numbers that are larger than $\bar{\gamma} > 2$ from voltage-induced buckling to a voltage-induced RPI. We thus performed a linear stability analysis of surface tension on the electromechanical deformation of the DE film. The analysis follows that previously performed,^{23,27} with the boundary conditions being different in the present work. To do so, we note that the total stress \mathbf{T} due to both mechanical deformation and electrical polarization of the DE is $\mathbf{T} = \mathbf{T}^M + \mathbf{T}^E$. Assuming a neo-Hookean material model, the mechanical and electrical stresses can be written as

$$\mathbf{T}^M = \frac{\mu}{J} \mathbf{B} - p \mathbf{1}, \quad (6)$$

$$\mathbf{T}^E = \epsilon \mathbf{E} \otimes \mathbf{E} - \frac{\epsilon}{2} |\mathbf{E}|^2 \mathbf{1},$$

where $\mathbf{B} = \mathbf{F}\mathbf{F}^T$ is the left Cauchy–Green strain tensor, $J = \det(\mathbf{F})$ and p is the hydrostatic pressure.

Stress in absence of body forces satisfies the equilibrium equation $\nabla \cdot \mathbf{T} = 0$. Assuming there is no free charge in the material, Gauss's law for an ideal linear DE, where electric displacement related to electric field *via* $\mathbf{D} = \epsilon \mathbf{E}$, reads as

$$\nabla \cdot \mathbf{D} = \epsilon (\nabla \cdot \mathbf{E}) = 0 \quad (7)$$

Consequently, we can obtain $\nabla \cdot \mathbf{T}^E = 0$, and as a result the equilibrium equation reduces to

$$\nabla \cdot \mathbf{T}^M = 0 \quad (8)$$

Because a linear stability analysis assumes small deformations in the DE film at instability, we next linearize the stress

expressions in (6). The left Cauchy–Green strain tensor \mathbf{B} for infinitesimal strains then can be approximated as

$$\mathbf{B} \approx \mathbf{1} + 2\boldsymbol{\varepsilon}, \quad (9)$$

where the strain tensor $\boldsymbol{\varepsilon} = \frac{1}{2}(\nabla\mathbf{u} + \nabla^T\mathbf{u})$ and $\mathbf{u} = (u_1 \ u_2)^T$ is the displacement vector. The perturbed expression of mechanical stress for an incompressible neo-Hookean material ($J = 1$) then becomes

$$\dot{\mathbf{T}}^M = \mu(\nabla\dot{\mathbf{u}} + \nabla^T\dot{\mathbf{u}}) - \dot{p}\mathbf{1} \quad (10)$$

The perturbed electrical stress is²⁷

$$\dot{\mathbf{T}}^E = 2\epsilon\dot{\mathbf{E}} \otimes \mathbf{E} - \epsilon(\dot{\mathbf{E}}\cdot\mathbf{E})\mathbf{1} \quad (11)$$

where $\dot{\mathbf{E}} = (\dot{E}_1 \ \dot{E}_2)^T$ is the perturbed electric field vector. At the onset of instability, the DE undergoes a small, symmetric sinusoidal undulation δH on both the top and bottom surfaces of the DE film. Consequently, one can obtain the electric field expression by performing a Taylor expansion

$$\frac{\Phi}{H + 2\delta H} = \frac{\Phi}{H} - 2\left(\frac{\Phi}{H}\right)\frac{\delta H}{H} + O(\delta H^2) \quad (12)$$

Therefore the perturbed electric field is $\dot{E}_2 = 2(\Phi/H^2)\delta H$, and by inserting it into (10) the perturbed electric stress for 2D plane-strain conditions becomes

$$\dot{\mathbf{T}}^E = 2 \begin{pmatrix} \frac{\Phi^2}{H^3}\delta H & 0 \\ 0 & -\epsilon\frac{\Phi^2}{H^3}\delta H \end{pmatrix} \quad (13)$$

3.2 Linear stability analysis

By inserting the perturbed state of stress in (10) into the stress equilibrium equation for the perturbed state in (8), that is $\nabla\cdot\dot{\mathbf{T}}^M = 0$, and enforcing the incompressibility condition $\nabla\cdot\dot{\mathbf{u}} = 0$, we can obtain the equilibrium equation at the perturbed state:

$$\mu\nabla^2\dot{\mathbf{u}} - \nabla\dot{p} = 0 \quad (14)$$

The boundary conditions on top of the beam are:

$$\dot{T}_{22} = 2\gamma\dot{\kappa}, \quad \dot{T}_{12} = 0, \quad \text{at } x_2 = H/2, \quad (15)$$

where the first term is the film subjected to the Young–Laplace boundary condition in which the mean curvature can be calculated as $\dot{\kappa} \approx \frac{1}{2}\frac{\partial^2\dot{u}_2}{\partial x_1^2}$. Due to symmetry of the DE film in the thickness direction, only the upper half of the film is considered, and the symmetry boundary conditions at $x_2 = 0$ can be written as

$$\dot{u}_2 = 0, \quad \frac{\partial^2\dot{u}_2}{\partial x_1^2} = 0, \quad \text{at } x_2 = 0. \quad (16)$$

The perturbed fields due to the incompressibility condition $\nabla\cdot\dot{\mathbf{u}} = 0$ are assumed to take the form of the stream function $\psi(x_1, x_2)$ such that

$$\dot{u}_1 = \frac{\partial\psi}{\partial x_2}, \quad \dot{u}_2 = -\frac{\partial\psi}{\partial x_1}. \quad (17)$$

We assume a sinusoidal morphology on the top and bottom surfaces of the film, which is characteristic of the RPI. Therefore, the stream function and hydrostatic pressure takes the following forms:

$$\begin{aligned} \psi(x_1, x_2) &= \tilde{\psi}(x_2) \sin(kx_1) \\ \dot{p}(x, y) &= \tilde{p}(x_2) \cos(kx_1). \end{aligned} \quad (18)$$

Inserting these relations into the governing equation in (14), we obtain the following sets of equations

$$\begin{aligned} -\mu k^2 \tilde{\psi}'(x_2) + \mu \tilde{\psi}'''(x_2) + k\tilde{p}(x_2) &= 0, \\ -\mu k^3 \tilde{\psi}(x_2) + k\tilde{\psi}''(x_2) + \tilde{p}'(x_2) &= 0, \end{aligned} \quad (19)$$

while first set of boundary conditions in (15) at $x_2 = H/2$ becomes

$$\begin{aligned} 2\mu k \tilde{\psi}'(H/2) + \gamma k^3 \tilde{\psi}(H/2) + \tilde{p}(H/2) - 2k \frac{\Phi^2}{H^3} \tilde{\psi}(H/2) &= 0, \\ \tilde{\psi}''(H/2) + k^2 \tilde{\psi}(H/2) &= 0, \end{aligned} \quad (20)$$

and the second set in (16) at $x_2 = 0$ becomes

$$\tilde{\psi}(0) = \tilde{\psi}''(0) = 0 \quad (21)$$

The solution to $\tilde{\psi}$ and \tilde{p} is

$$\begin{aligned} \tilde{\psi}(x_2) &= \frac{k \cosh(kx_2)(2C_2k\mu + C_1x_2)}{2k^2\mu} \\ &\quad - \frac{\sinh(kx_2)(k\mu(C_2k^2x_2 - C_4x_2 - 2C_3) + C_1)}{2k^2\mu} \end{aligned} \quad (22)$$

$$\tilde{p}(x_2) = \mu(C_4 - C_2k^2)\sinh(kx) + C_1\cosh(kx) \quad (23)$$

Inserting the expressions for $\tilde{p}(x_2)$ and $\tilde{\psi}(x_2)$ into the four boundary conditions in (20) and (21), we obtain a set of four linear algebraic equations for four unknowns:

$$\mathbb{A} \begin{pmatrix} C_1 \\ C_2 \\ C_3 \\ C_4 \end{pmatrix} = 0 \quad (24)$$

where \mathbb{A} is a 4×4 matrix. The existence of a non-trivial solution requires

$$\det \mathbb{A} = 0 \quad (25)$$

By solving the equation in (25), we can obtain expressions for both the normalized voltage

$$\bar{\Phi}^2 = \frac{Hke^{Hk}(Hk(2 - \bar{\gamma}) + Hk\bar{\gamma} \cosh(Hk) + 2 \sinh(Hk))}{(-1 + e^{Hk})^2} \quad (26)$$

and also the elastocapillary number $\bar{\gamma}$:

$$\bar{\gamma} = \frac{2\bar{\Phi}^2}{H^2k^2} - \frac{\cosh^2\left(\frac{Hk}{2}\right)(Hk + \sinh(Hk))}{k \sinh^2\left(\frac{Hk}{2}\right)} \quad (27)$$

where $\bar{\Phi} = (\Phi/H)\sqrt{\epsilon/\mu}$ and $\bar{\gamma} = \gamma/\mu H$ is the elastocapillary number.

3.3 Discussion

Having now obtained the normalized critical voltage $\bar{\Phi}_c$ for the electromechanical buckling instability in eqn (5) and the electroelastocapillary RPI in eqn (26), where the lowest normalized electric voltage in each curve gives the critical voltage (Fig. 3), we plot both solutions in Fig. 2, along with FE simulation results for different elastocapillary numbers $\bar{\gamma}$. First, we note that the critical voltage for buckling increases nonlinearly with increasing elastocapillary number. However, the critical voltage for the RPI is a constant, *i.e.* $\bar{\Phi}_c = 2$ (Fig. 3), therefore, for a critical elastocapillary number of $\bar{\gamma}_c \simeq 2$ (Fig. 2), the instability mechanism transitions from buckling to RPI. As can be seen, the FE simulations capture both the critical buckling and critical RPI voltages, along with accurately capturing the elastocapillary number at which the instability transition occurs.

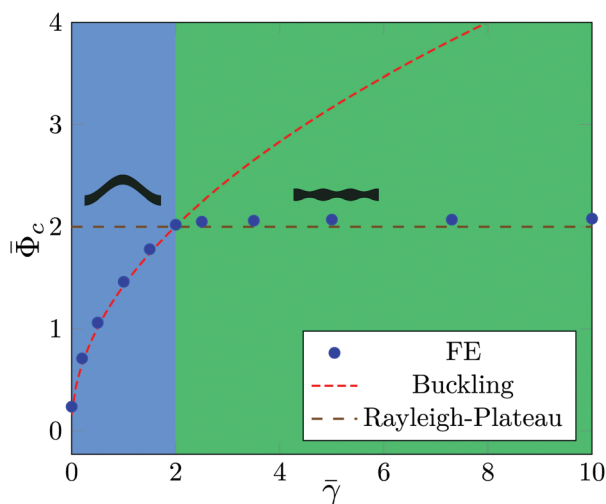


Fig. 2 Critical voltage vs. elastocapillary number showing the transition between buckling to RPI at $\bar{\gamma} = \gamma_c/\mu H = 2$.

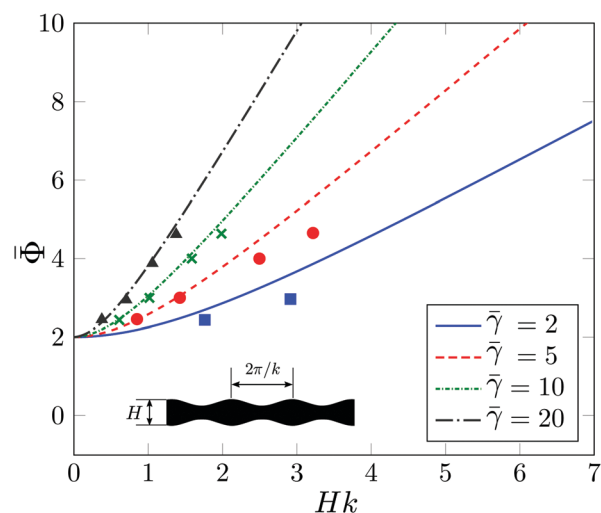


Fig. 3 The voltage for inducing RPI for a DE film as a function of elastocapillary number. The lowest electric potential which gives the critical value for each curve is a constant $\bar{\Phi}_c = 2$. Solid lines are analytic solution, symbols are FE simulation results.

There are three important factors that impact the electroelastocapillary instability transition from buckling to RPI: multiphysical coupling, *i.e.* electroelasticity and elastocapillarity, the geometry of the DE film, and the boundary conditions. We first discuss the effect of the DE film geometry. To do so, we first note that the total energy of the system can be written as

$$\Pi = E_m + E_e + E_s \quad (28)$$

where E_m is the elastic energy, E_e is the electrical energy and E_s is the surface energy. The total surface energy of both surfaces can be computed as

$$E_s = 2\gamma \int_0^L \sqrt{1 + \left(\frac{du_2}{dx_1}\right)^2} dx_1 \quad (29)$$

Expanding this energy for the onset of instability where the surface undergoes small deformation, the surface energy functional is approximated as

$$E_s \simeq 2L\gamma + \frac{\gamma k^6 L^3 \bar{\psi}(x_2)^2}{3} \quad (30)$$

From eqn (30), one can see that the second term is always positive, and therefore the minimum of E_s is where $k \rightarrow 0$. This implies that in the absence of an electric field, *i.e.* $\bar{\Phi} = 0$ or $E_e = 0$, the surface energy when the DE film is flat $E_s = 2L\gamma$ does not decrease the total energy of the system, and therefore no elastocapillary or RPI will occur for plane-strain DE films, regardless of the magnitude of the surface tension. This is of course different from previous studies of RPI in cylindrical geometries of radius R_0 , where a critical elastocapillary number of $\gamma = 6\mu R_0$ was obtained,^{6,10,28} and demonstrates the impact of the DE geometry on the RPI.

As the above analysis demonstrates that the RPI cannot occur for the plane-strain geometries that characterize DE films, we now discuss the effect of multiphysical coupling through the electric fields that are applied to actuate DEs. When no electric fields are present, the minimum energy configuration of the DE film is one in which it is flat. However, once an electric field is applied to the DE film, the total energy decreases, because the electrical energy contribution is

$$E_e = - \int_{-H/2}^{H/2} \int_0^{L_1} \frac{1}{2} \epsilon |\mathbf{E}|^2 dA \quad (31)$$

Therefore, the decrease of the electrostatic potential energy of the system from the initially flat state $E_e = -\epsilon L \Phi^2 / 2H$ creates the possibility of an electro-elastocapillary instability. For smaller elastocapillary numbers ($\bar{\gamma} < 2$), the DE film shows the buckling instability, which results in an increase in surface area along the top and bottom surfaces due to the dominance of the elastic energy over the surface energy. When $\bar{\gamma} > 2$, the elastocapillary number is sufficiently large, which creates sufficient driving force to prevent electromechanically-driven instability modes like buckling that lead to surface area increases. This makes the RPI mechanism a viable one, even in the presence of an applied electric field.

While the electric field and geometry couple to alter the critical elastocapillary number for RPI in DEs as compared to

previous studies of RPI in soft solids, we now examine the question of the instability wavelength for the RPI in DEs. Based on eqn (26), we plot the normalized voltage as a function of wavenumber Hk in Fig. 3, where $k = 2\pi/l$ and l being the wavelength. We find the long-wavelength ($k \rightarrow 0$) mode becomes unstable first (the minimum of plots in Fig. 3) at $\bar{\Phi}_c = 2$, which occurs for all elastocapillary numbers, implying that the electro-elastocapillary RPI in the DEs is an infinite wavelength instability. This result is similar to that found previously in analyses of the instability wavelength in RPIs in soft solids, where the only driving force is elastocapillary.^{6,10,28}

We note that in our FE simulations, because we ramped up the voltage slowly to mimic quasistatic loading, we only observe long wavelengths at instability, corresponding to $Hk \rightarrow 0$ in Fig. 3, due to the fact that the RPI occurs when $\bar{\Phi}$ reaches 2. However, we did verify that, when constant voltage loadings exceeding $\bar{\Phi} = 2$ were chosen for various elastocapillary numbers, we did observe smaller wavelengths for the RPI in line with the analytic predictions shown in Fig. 3. Specifically, the wavelengths obtained from the FE simulations are plotted against the analytic solutions in Fig. 3, while examples of finite wavelength RPI instabilities that were obtained for $\bar{\Phi} > \bar{\Phi}_c$ are shown in Fig. 4. As can be seen in Fig. 4, the wavelength of the RPI decreases with increasing voltage for a constant elastocapillary number, matching the analytic predictions in Fig. 3.

Finally, we note that the mechanical boundary conditions, or the ways in which the DE film is constrained, play an important role in determining the electro-elastocapillary instability that is observed. For example, recent experiments²³ and computational studies¹⁹ considered DE films similar to the one in Fig. 1, though with the bottom surface fixed in addition to both ends. By considering surface tension effects on the top surface, and applying a voltage difference similar to that shown in Fig. 1, an interesting surface instability transition from creasing at low elastocapillary numbers to longer wavelength wrinkling above a critical elastocapillary number was observed. The constraint at the bottom of the DE film thus prevents the RPI, which requires instabilities on both the top and bottom surfaces, from occurring.

We also note that the analytic solutions and FE simulations performed in this work were for 2D, plane strain conditions,

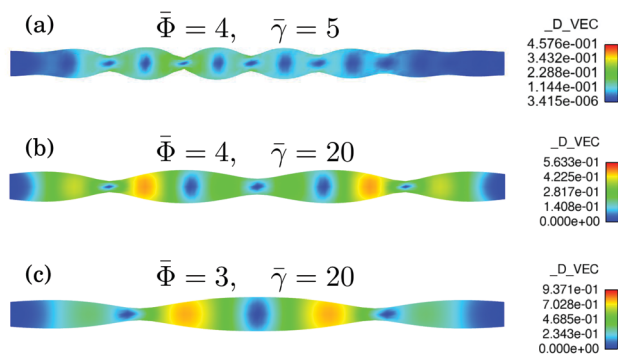


Fig. 4 Snapshots of RPI instability for voltages $\bar{\Phi} > \bar{\Phi}_c$ and different elastocapillary numbers $\bar{\gamma}$.

which implies that there is no out of plane deformation. Therefore, it is to be determined in future work whether the conclusions drawn in this work are valid when the full 3D picture is considered.

4 Conclusion

In conclusion, we have demonstrated that Rayleigh–plateau instabilities can be induced in electroactive polymers like dielectric elastomers under 2D plane strain conditions. The effect is driven by the driving force to find different instability modes that reduce the surface area, as compared to those that would otherwise occur in the absence of surface tension. Our finite element simulations were able to replicate our analytic models in predicting the instability transition from buckling to Rayleigh–plateau at a critical normalized voltage of $\bar{\Phi}_c = 2$, and a critical elastocapillary number of $\bar{\gamma}_c \simeq 2$. Our results shed light on the effects of geometry and multiphysical couplings on the Rayleigh–plateau instability in soft solids, and the interesting physics observed in the electro-elastocapillary mechanics of electroactive polymers.

Acknowledgements

H. S. P. and S. S. acknowledge funding from the ARO, grant W911NF-14-1-0022.

References

- 1 L. Rayleigh, *Proc. London Math. Soc.*, 1878, **10**, 4–13.
- 2 B. Roman and J. Bico, *J. Phys.: Condens. Matter*, 2010, **22**, 493101.
- 3 B. Andreotti, O. Baumchen, F. Boulogne, K. E. Daniels, E. R. Dufresne, H. Perrin, T. Salez, J. H. Snoeijer and R. W. Style, *Soft Matter*, 2016, **12**, 2993–2996.
- 4 R. W. Style, A. Jagota, C.-Y. Hui and E. R. Dufresne, 2016, arXiv:1604.02052.
- 5 J.-L. Liu and X.-Q. Feng, *Acta Mech. Sin.*, 2012, **28**, 928–940.
- 6 S. Mora, T. Phou, J.-M. Fromental, L. M. Pismen and Y. Pomeau, *Phys. Rev. Lett.*, 2010, **105**, 214301.
- 7 B. Barriere, K. Sekimoto and L. Leibler, *J. Chem. Phys.*, 1996, **22**, 1735–1738.
- 8 P. Cialletta and M. B. Amar, *Soft Matter*, 2012, **8**, 1760–1763.
- 9 M. Taffetani and P. Ciarletta, *J. Mech. Phys. Solids*, 2015, **81**, 91–120.
- 10 C. Xuan and J. Biggins, *Phys. Rev. E*, 2016, **94**, 023107.
- 11 F. Carpi, S. Bauer and D. D. Rossi, *Science*, 2010, **330**, 1759–1761.
- 12 E. Biddiss and T. Chau, *J. Biomed. Eng.*, 2008, **30**, 403–418.
- 13 P. Brochu and Q. Pei, *Macromol. Rapid Commun.*, 2010, **31**, 10–36.
- 14 D. Rus and M. T. Tolley, *Nature*, 2015, **521**, 467–475.
- 15 S. Kim, C. Laschi and B. Trimmer, *Trends Biotechnol.*, 2013, **31**, 287–294.
- 16 F. Carpi, G. Frediani, S. Turco and D. De Rossi, *Adv. Funct. Mater.*, 2011, **21**, 4152–4158.

- 17 D. P. Holmes, B. Tavakol, G. Froehlicher and H. A. Stone, *Soft Matter*, 2013, **9**, 7049–7053.
- 18 F. Carpi, A. Khanicheh, C. Mavroidis and D. De Rossi, *IEEE/ASME Trans. Mechatron.*, 2008, **13**, 370–374.
- 19 S. Seifi and H. S. Park, *Int. J. Solids Struct.*, 2016, **87**, 236–244.
- 20 M. Biot, *Mechanics of incremental deformations: theory of elasticity and viscoelasticity of initially stressed solids and fluids, including thermodynamic foundations and applications to finite strain*, Wiley, 1965.
- 21 R. W. Ogden, *Non-linear elastic deformations*, 1997.
- 22 H. S. Park and T. D. Nguyen, *Soft Matter*, 2013, **9**, 1031–1042.
- 23 Q. Wang and X. Zhao, *Phys. Rev. E: Stat., Nonlinear, Soft Matter Phys.*, 2013, **88**, 042403.
- 24 R. Pelrine, R. Kornbluh, Q. Pei and J. Joseph, *Science*, 2000, **287**, 836–839.
- 25 J. He and C. M. Lilley, *Nano Lett.*, 2008, **8**, 1798–1802.
- 26 G.-F. Wang and X.-Q. Feng, *Appl. Phys. Lett.*, 2007, **90**, 231904.
- 27 S. Seifi and H. S. Park, 2016, arXiv:1611.06419, arXiv preprint.
- 28 M. Taffetani and P. Ciarletta, *Phys. Rev. E: Stat., Nonlinear, Soft Matter Phys.*, 2015, **91**, 032413.